11th International Symposium on Turbulence and Shear Flow Phenomena (TSFP11)
Southampton, UK, July 30 to August 2, 2019

TURBULENT TRANSPORT IN THE NEAR FIELD OF SWIRLING JETS

Vladimir Dulin

Kutateladze Institute of Thermophysics
Siberian Branch of the Russian Academy of Sciences
1 Lavrentyev Avenue, Novosibirsk, Russia
vmd@itp.nsc.ru

Aleksei Lobasov

Kutateladze Institute of Thermophysics
Siberian Branch of the Russian Academy of Sciences
1 Lavrentyev Avenue, Novosibirsk, Russia
alexey.lobasov@gmail.com

Dmitriy Markovich

Kutateladze Institute of Thermophysics
Siberian Branch of the Russian Academy of Sciences
1 Lavrentyev Avenue, Novosibirsk, Russia
dmark@itp.nsc.ru

Kemal Hanjalic

Chemical Engineering Department
Delft University of Technology
58, Van der Maasweg 9, Delft, The Netherlands
khanjalic@gmail.com

ABSTRACT

We report on the experimental study of turbulent transport in the near field of swirling jets at Re = 5000 by using simultaneously the stereoscopic particle image velocimetry and planar laser-induced fluorescence methods. The present focus is on the analysis of terms of the mean (axial) momentum and scalar (mass) transport equations, estimated from the mean velocity and concentration, the Reynolds stress and turbulent flux components, measured in the central axial plane of the jets. A proper orthogonal decomposition has also been applied to the velocity data sets to analyse contribution of the coherent velocity and scalar fluctuations to the turbulent momentum and mass fluxes for different swirl rates.

INTRODUCTION

Swirl is often superimposed to jet flows to promote mixing and heat and mass transfer in the initial region of the flow (Gupta et al., 1984; Fröhlich et al., 2008; Zemtsop et al., 2009; Cozzi et al., 2018). Whereas ring-like vortices are formed in the shear layer of the non-swirling and weakly swirling jets, helical vortex structures appear in the mixing layer of strongly swirling jets and are considered to enhance mixing (McIlwain and Pollard, 2002; Loiseleux and Chomaz, 2003; Liang and Maxworthy, 2005; Zemtsop et al., 2009; Markovich et al., 2016). When the swirl rate exceeds a certain critical value, a breakdown of the vortex occurs in swirling jets (Billant et al., 1998; Lucca-Negro and O'doherty, 2001; Loiseleux and Chomaz, 2003; Liang and Maxworthy, 2005; Oberleithner et al., 2012). Vortex breakdown corresponds to the formation of a wake region or an unsteady recirculation zone in the vortex core, which intensifies mixing dramatically.

Oberleithner et al. (2012) have suggested that an increase of the jet swirl rate leads first to the formation of an intermittent central recirculation zone, which with a further increase of the swirl rate becomes permanent. The formation of the central recirculation zone gives rise to a global flow instability with a helical mode, corresponding to precession of the swirling jet (see also Liang and Maxworthy, 2005). From conditionally sampled pointwise 2D and 3D velocity measurements Cala et al. (2006), Legrand et al. (2010), Markovich et al. (2016) have detect a coherent structure in a high-swirl jet, consisting of a spiralling vortex core and secondary helical large-scale vortex structures in the inner and outer mixing layers. However, comparable experimental studies and quantitative analysis of mixing and the role of large-scale coherent structures in scalar transport in swirling turbulent jets are still scarce in the literature.

The present paper reports on the application of PIV and PLIF techniques to quantify turbulent transport in the initial region of turbulent swirling jets for various swirl rates. The contribution of coherent velocity fluctuations to turbulent transport is evaluated using proper orthogonal decomposition.

EXPERIMENTAL SETUP

The jet flows were organized by an axisymmetric contraction nozzle. To induce flow swirl, a changeable vane swirler was mounted inside the nozzle (Alekseenko et al., 2012). Using swirlers with different inclination angles of the vanes, the considered swirl rate S (the definition is taken from Gupta et al. 1984) was 0.41, 0.7 and 1.0.

$$S = \frac{2}{3}\left(\frac{1-\left(d_1/d_2\right)^3}{1-\left(d_1/d_2\right)^2}\right)\tan\left(\psi\right) \qquad (1)$$

Here, $d_1 = 7$ mm is the diameter of the centre body supporting the vanes, $d_2 = 27$ mm is the external diameter of the swirler, and ψ is the vanes inclination angle relatively to the axis. The nozzle exit diameter d was 15 mm. The Reynolds number, defined as $\mathrm{Re} = U_0 d/\nu$ (where U_0 is the bulk flow velocity of the jet; ν is the air kinematic viscosity), was 5 000.

The air flow was supplied from a pressure line, and its flow rate was precisely controlled by mass flow-meters (Bronkhorst). An acetone seeder was used to introduce acetone vapour (serving as the reference scalar) into the air flow. The jet issued from the nozzle was also seeded by 0.5 μm TiO_2 by using a chamber with mechanical mixer. The surrounding air was seeded by a fog machine.

A double-head Nd:YAG laser (Quantel, EverGreen) was used to illuminate the tracer particles for the PIV measurements. The laser beam was converted into a collimated laser sheet with the width of 50 mm and thickness less than 0.8 mm by using a system of cylindrical and spherical lenses. The fourth harmonic (266 nm) of a pulsed Nd:YAG laser (Quantel, Brilliant B) was used for the acetone PLIF excitation. A small portion of the laser radiation was directed to a power meter using a semi-transparent mirror. The PLIF laser beam was

aligned with that of the PIV system by using a dichroic mirror and converted to a collimated laser sheet.

Particle images were captured by a pair of CCD cameras (Bobcat ImperX IGV-B2020 with sensor size of 2048×2048 pixels). A narrow band-pass optical filter (532 nm ± 10 nm) was mounted on the cameras. An UV-sensitive image intensifier (LaVision IRO) was used to image local fluorescence intensity of the acetone vapour. The intensifier was equipped with a quartz lens (LaVision, f # 2.8, 100 mm) and optical band-pass filter (300-320 nm). The images were recorded by a sCMOS camera (16-bit with sensor size of 2560 × 2160 pixels). An additional ICCD camera (PCO DicamPro) was used to monitor the spatial distribution of the laser sheet intensity for each pulse of the PLIF laser by using a quartz cuvette, filled with a uniform solution of a fluorescent dye (Rhodamine 6G).

DATA PROCESSING

The PIV images were processed by an in-house software "ActualFlow". For evaluation of the local displacement of the tracers, an iterative cross-correlation algorithm with continuous shift and deformation of interrogation areas (Scarano, 2002) was used. After four iterations, the size of the integration areas was reduced from 64×64 to 32×32 pixels. The spatial overlap rate between the interrogation areas was 50%. Spatial calibration of the stereo PIV and PLIF cameras was performed by obtaining a third-order polynomial transforms for each camera. This was done by processing images of a plane calibration target placed in the region of interest for five different positions in the normal-to-plane direction with the step of 0.5 mm.

To process PLIF data a number of routines was used. The background signal, produced by dark current and thermal noise of the sensors, reflections and background luminosity, was evaluated by capturing PLIF images without jet flow (but with laser pulses) and was subtracted from the original PLIF images with the jet. Also, correction of the non-uniform spatial sensitivity of the detector was performed by using an image of a white paper sheet, placed out of focus.

To reveal coherent structures in the flows, the fluctuating velocity data set [$\mathbf{u}'(\mathbf{x}, t_1)\ldots\mathbf{u}'(\mathbf{x}, t_N)$] for each flow case was processed by a snapshot proper orthogonal decomposition (POD) method (Sirovich, 1987). The decomposition into a series of orthonormal POD modes [$\boldsymbol{\varphi}_1(\mathbf{x})\ldots\boldsymbol{\varphi}_N(\mathbf{x})$], multiplied by normalized temporal coefficients $a_q(t)$, is based on a singular value decomposition:

$$\mathbf{u}'(\mathbf{x},t_k)=\sum_{q=1}^{N}\alpha_q(t_k)\sigma_q\boldsymbol{\varphi}_q(\mathbf{x}) \qquad (2),$$

$$\text{where } \sum_{k=1}^{M}\boldsymbol{\varphi}_i(\mathbf{x}_k)\boldsymbol{\varphi}_j(\mathbf{x}_k)=\delta_{ij} \text{ and } \sum_{k=1}^{N}\alpha_i(t_k)\alpha_j(t_k)=\delta_{ij} \quad (3)$$

The singular values σ_q are positive and listed in the descending order. They characterize amplitudes of the modes and correspond to the square root of POD eigenfunctions λ, used in another common notation.

Since, each POD mode can be expressed as a linear combination of the velocity fields (4), coherent fluctuations of the velocity and concentration of passive scalar, corresponding to this mode, can be evaluated from the phase-averaging (5) (Legrand et al., 2010).

$$\boldsymbol{\varphi}_q(\mathbf{x})=\sum_{k=1}^{N}a_{qk}\mathbf{u}'(\mathbf{x},t_k)\sigma_q^{-1} \qquad (4)$$

$$\hat{\mathbf{u}}_q(\mathbf{x})=\left(\sigma_q/\sqrt{N}\right)\boldsymbol{\varphi}_q(\mathbf{x}),\ \hat{c}_q(\mathbf{x})=\left(1/\sqrt{N}\right)\sum_{k=1}^{N}a_{qk}c'(\mathbf{x},t_k) \quad (5)$$

RESULTS

Figure 1 shows the time-averaged velocity and concentration distributions for the studied jets (S = 0, 041 and 1.0). Figure 2 and 3 show distributions of the Reynolds stresses and turbulent mass fluxes, respectively. For the case S = 0.41 (referred to as low-swirl jet) a wake region is present at the jet axis, where the average axial velocity remains positive. For S = 1.0 (referred to as high-swirl jets) the black solid line surrounds the region with negative values of the mean axial velocity, corresponding to a central recirculation zone.

In general, there are two mixing layers in the swirling jets, viz., the inner mixing layer between the annular swirling jet and the recirculation/wake region and the outer mixing layer between the jet and the surrounding air. Transverse turbulent scalar mass flux is found to be most intensive in the outer mixing layers. In the inner mixing layer, the amplitude of the Reynolds stress increases with the swirl rate. For the jets with vortex breakdown the stress reaches the highest values in the inner mixing layer close to the nozzle exit. Also, it is found that the radial fluxes are in a good agreement with the mean velocity and concentration gradients respectively, thus justifying the gradient-based turbulent transport models for the radial direction.

Figure 4 shows profiles of the terms of the mean mass transport equation (6) for different cross-sections y/d, which intersect both the wake region of the low-swirl jet and recirculation zone of the high-swirl jet. Term on the right-hand-side of the equation corresponds to the molecular diffusion and is found to be negligibly small in comparison to the other terms, thus not plotted. The residual term is plotted in Figure 4 to demonstrate the measurements error. It appears to be reasonably small.

$$U_y\frac{\partial C}{\partial y}+U_r\frac{\partial C}{\partial r}+\frac{\partial\langle u_y'c'\rangle}{\partial y}+\frac{\partial\langle u_r'c'\rangle r}{r\partial r}=D\Delta C \qquad (6)$$

In general, the contribution of the third term, corresponding to the turbulent diffusion in the axial direction, for the considered cross-sections is found to be small in comparison to the other terms. For the non-swirling jet, the axial advection term appears to be almost completely compensated by the turbulent transport in the radial direction. Contribution of the radial advection increases with the swirl rate and for the high-swirl case reaches almost the same amplitude as that of the axial advection and radial turbulent diffusion.

Figure 5 shows profiles of terms of the axial mean momentum transport equation (7) for the same cross-sections as in Figure 4. Terms on the right-hand-side of the equation correspond to the mean pressure gradient and viscous diffusion. The latter one is found to be negligibly small in comparison to the other terms. Thus, the residual term in Figure 4 corresponds to the mean pressure gradient ($\rho^{-1}\partial P/\partial y$).

$$U_y\frac{\partial U_y}{\partial y}+U_r\frac{\partial U_y}{\partial r}+\frac{\partial\langle u_y'^2\rangle}{\partial y}+\frac{\partial\langle u_r'u_y'\rangle r}{r\partial r}=-\frac{\partial P}{\rho\partial y}+\nu\Delta U_y \quad (7)$$

In the mixing layer of the non-swirling jet, effect of the axial advection appears to be opposite to that of the radial diffusion. Radial advection has comparable amplitude and acts as a sink term in the mixing layer. For the swirling jets, the residual term shows that the mean pressure gradient has the highest magnitude near the jet axis (at the vortex core) and is compensated by the radial turbulent diffusion. The radial advection increases in the inner shear layer of the swirling jets, especially after formation of the central recirculation zone. For the high-swirl jet with vortex breakdown, the transport terms have much greater magnitude in comparison to those for the other flow cases.

Figure 6 shows the POD spectra of the velocity fluctuations for the jets with different swirl rates. For the high-swirl jet with vortex breakdown (S = 1.0), there are two most energetic POD modes. They contain approximately 16% of the spatial-averaged turbulent kinetic energy, whereas the energy of the rest modes is below 2%. Values of the temporal coefficients for the first two modes for S = 1.0 are scattered around a circle-like plot, indicating that these modes are statistically correlated. For the non-swirling flow, there is also a pair of the first POD modes with energy noticeably greater than those of the rest modes (above 25%). For the low-swirl jet, energy of the POD modes decreases monotonously.

Spatial distributions of the POD modes for the jets and phase-averaged fluctuations of the passive scalar concentration are shown in Figure 7. For the non-swirling and high-swirl jets the first two POD modes correspond to large-scale vortex structures, whereas for the low-swirl jet they correspond to local flow fluctuations in the wake region. Large-scale vortex structures in the latter case are found in the third and fourth mode; thus, the third POD mode is plotted for the low-swirl jet.

For the non-swirling and low-swirl jets, the POD modes show almost symmetrical formation of large-scale vortex structures in the mixing layers. They grow downstream and induce coherent fluctuations of the concentration in a form of travelling waves. The first and second (not shown) POD modes are found to be shifted by the phase angle of $\pi/2$. They are expected to be related to toroidal vortices. The first two POD modes for the high-swirl jets with vortex breakdown (only the first mode is shown) correspond to large-scale vortex structures both in the inner and outer mixing layer. The vortex structures induce concentration fluctuations in the outer mixing layer and appear to be located in an asymmetric manner relatively to the jet axis. They are expected to correspond to helical structures.

Contribution of the coherent velocity fluctuations to the Reynolds stress $\langle u'_x u'_y \rangle$ (Figure 8 and 9) has been evaluated in frames of the triple decomposition $u' = \hat{u} + u''$, where $\hat{u}$ and u'' are the coherent and 'background' velocity fluctuations, respectively. The former ones are obtained from the phase-averaging by using the temporal coefficients of the POD modes ($\hat{u}_1$ and $\hat{u}_2$ for the non-swirling and high-swirl jets, and $\hat{u}_3$ and $\hat{u}_4$ for the low-swirl jet). It has been verified that $\langle \hat{u}_x u''_y \rangle + \langle u''_x \hat{u}_y \rangle$ is equal to zero. The same was done for the Reynolds flux $\langle u'_x c' \rangle$ (Figure 10 and 11). Contribution of coherent fluctuations to the Reynolds stress does not exceed 25% for the non-swirling and low-swirl jets. For the high-swirl jet with vortex breakdown the contribution to Reynolds stress and fluxes exceeds 50% for the considered cross-section.

CONCLUSIONS

Local transport of the axial momentum and scalar (mass) in the near field of turbulent swirling jets has been evaluated on the basis of PIV and PLIF measurements. Based on the POD decomposition, contribution of coherent structures to turbulent transport has been quantified. In general, breakdown of the vortex core for the high swirl jet provides dramatic increase of turbulent momentum and mass fluxes near the nozzle exit, with contribution of coherent fluctuations above 50%.

ACKNOWLEDGEMENTS

The research is supported by the Russian Science Foundation (grant No 16-19-10566).

REFERENCES

Billant, P., Chomaz, J.M., and Huerre, P., 1998, "Experimental study of vortex breakdown in swirling jets", *Journal of Fluid Mechanics*, Vol. 376, pp, 183-219.

Cala, C.E., Fernandes, E., Heitor, M.V., and Shtork S.I., 2006, "Coherent structures in unsteady swirling jet flow", *Experiments in Fluids*, Vol. 40, pp. 267-276.

Cozzi, F., Coghe, A., and Sharma, R., 2018, "Analysis of local entrainment rate in the initial region of isothermal free swirling jets by Stereo PIV", *Experimental Thermal and Fluid Science*, Vol. 94, pp. 281-294.

Fröhlich, J., García-Villalba, M., and Rodi, W., 2008, "Scalar mixing and large-scale coherent structures in a turbulent swirling jet", *Flow, Turbulence and Combustion*, Vol. 80, pp. 47-59.

Gupta, A.K., Lilley, D.G., and Syred, N., 1984, *Swirl Flows*. Abacus Press, Kent.

Legrand, M., Nogueira, J., Lecuona, A., Nauri, S., and Rodríguez, P.A., 2010, "Atmospheric low swirl burner flow characterization with stereo PIV", *Experiments in Fluids*, Vol. 48, pp. 901-913.

Liang, H., and Maxworthy, T., 2005, "An experimental investigation of swirling jets", *Journal of Fluid Mechanics*, Vol. 525, pp. 115-159.

Loiseleux, T., and Chomaz, J.M., 2003, "Breaking of rotational symmetry in a swirling jet experiment", *Physics of Fluids*, Vol. 15, pp. 511-523.

Lucca-Negro, O., and O'doherty, T., 2001, "Vortex breakdown: a review", *Progress in Energy and Combustion Science*, Vol. 27, pp. 431-481.

Markovich, D.M., Dulin, V.M., Abdurakipov, S.S., Kozinkin, L.A., Tokarev, M.P., and Hanjalić, K., 2016, "Helical modes in low-and high-swirl jets measured by tomographic PIV", *Journal of Turbulence*, Vol. 17, pp. 678-698.

McIlwain, S., and Pollard, A., 2002, "Large eddy simulation of the effects of mild swirl on the near field of a round free jet", *Physics of Fluids*, Vol. 14, pp. 653-661.

Oberleithner, K., Paschereit, C.O., Seele, R., and Wygnanski, I., 2012, "Formation of turbulent vortex breakdown: intermittency, criticality, and global instability", *AIAA Journal*, Vol. 50, pp. 1437-1452.

Scarano, F., 2002, "Iterative image deformation methods in PIV", *Measurement Science and Technology*, Vol. 13, pp. R1-R19.

Sirovich, L., 1987, "Turbulence and the dynamics of coherent structures. I. Coherent structures", *Quarterly of Applied Mathematic*, Vol. 45, pp. 561-571.

Zemtsop, C.P., Stöllinger, M.K., Heinz, S., and Stanescu, D., 2009, "Large-eddy simulation of swirling turbulent jet flows in absence of vortex breakdown", *AIAA Journal*, Vol. 47, pp. 3011-3021.

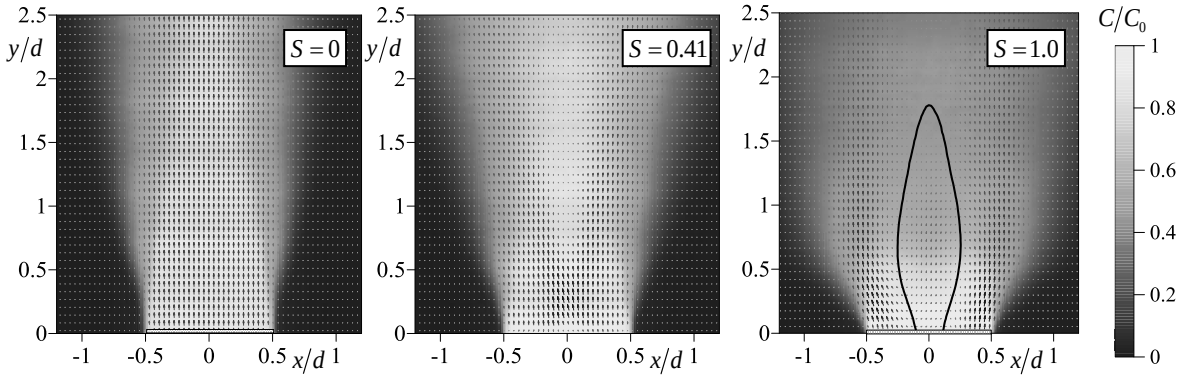

Figure 1. Distributions of the time-averaged velocity and concentration for swirling jets. Black solid line includes region with negative axial velocity

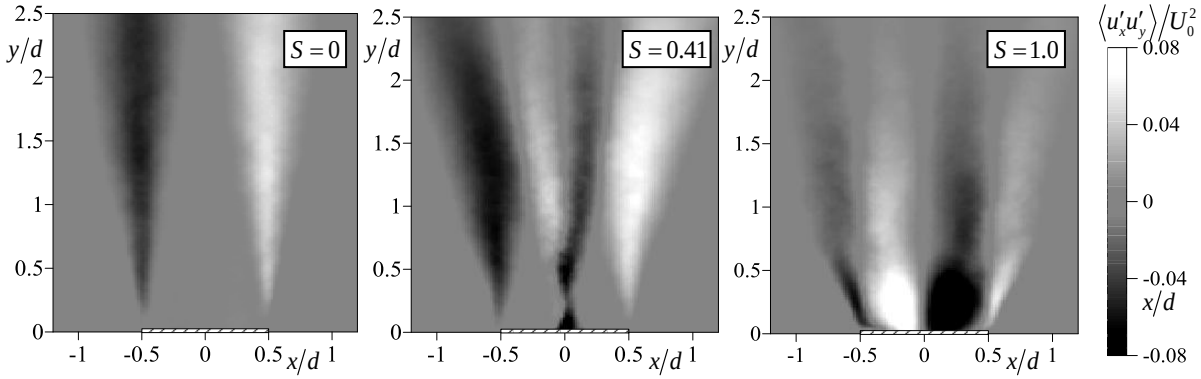

Figure 2. Distributions of the Reynolds stress for swirling jets

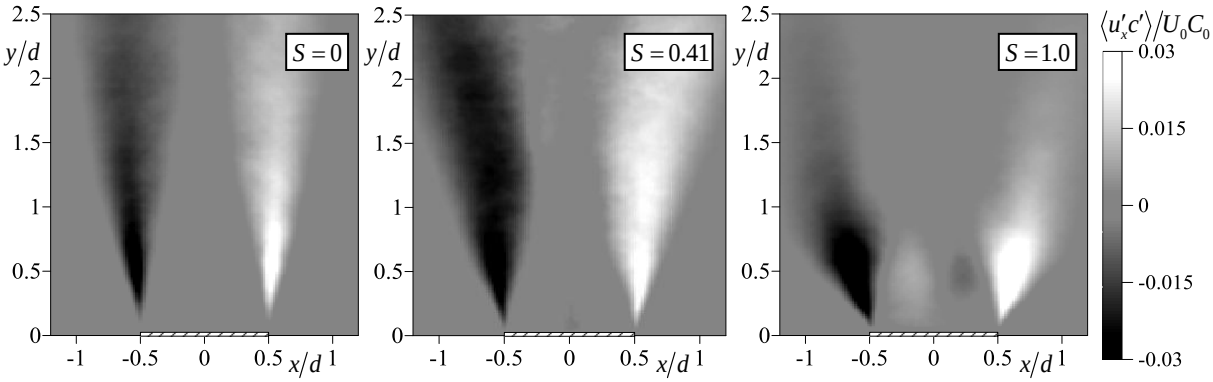

Figure 3. Distributions of the transversal turbulent flux of passive scalar for swirling jets

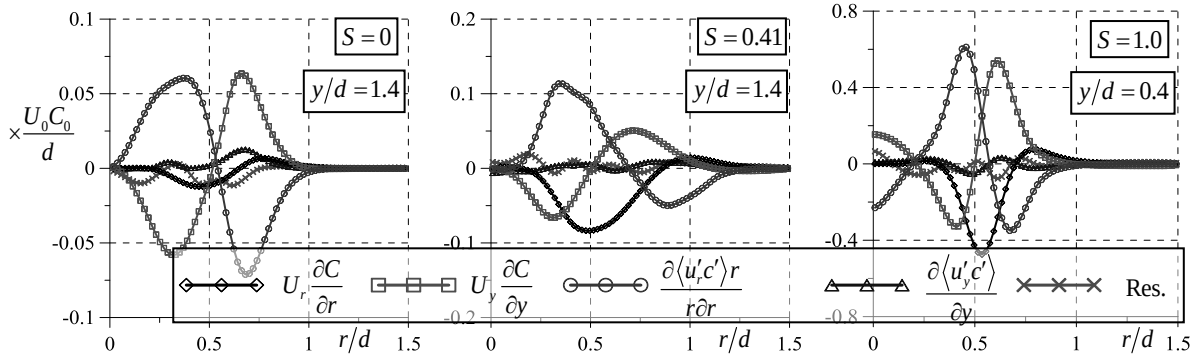

Figure 4. Terms of the mean scalar mass transport equation for swirling jets

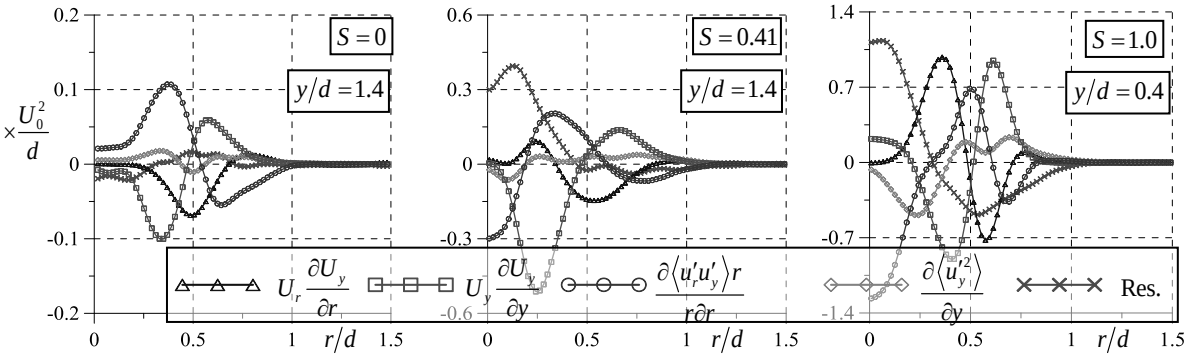

Figure 5. Terms of the axial mean momentum transport equation for swirling jets

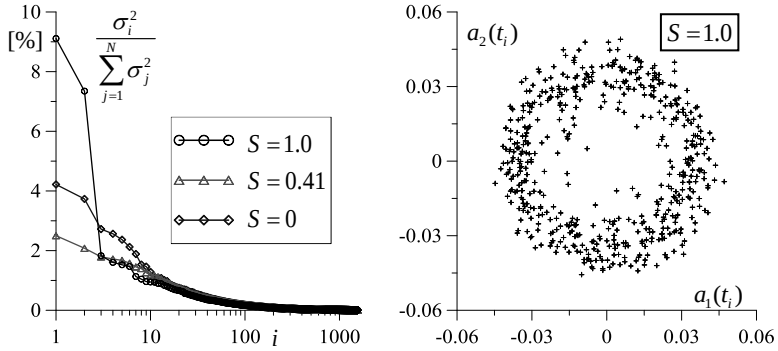

Figure 6. POD spectra for swirling jets and temporal coefficients for the first two POD modes for the high-swirl jet

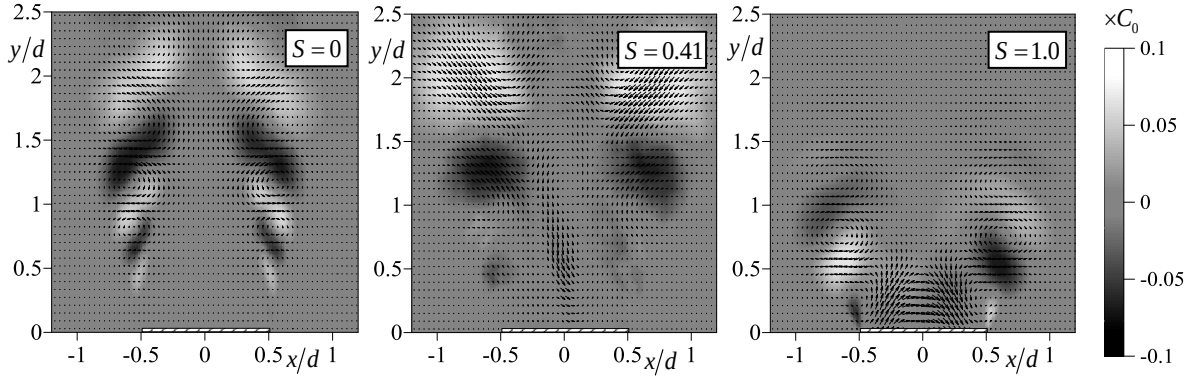

Figure 7. POD modes of the velocity fluctuations (first for $S = 0$ and 1.0, third for $S = 0.41$) and corresponding phase-averaged fluctuations of the passive scalar concentration for swirling jets

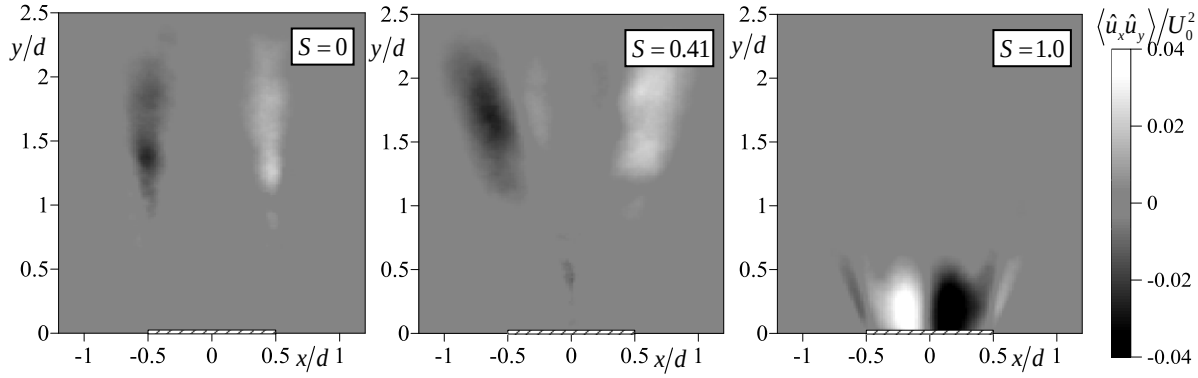

Figure 8. Contribution of coherent velocity fluctuations to the Reynolds stress for swirling jets

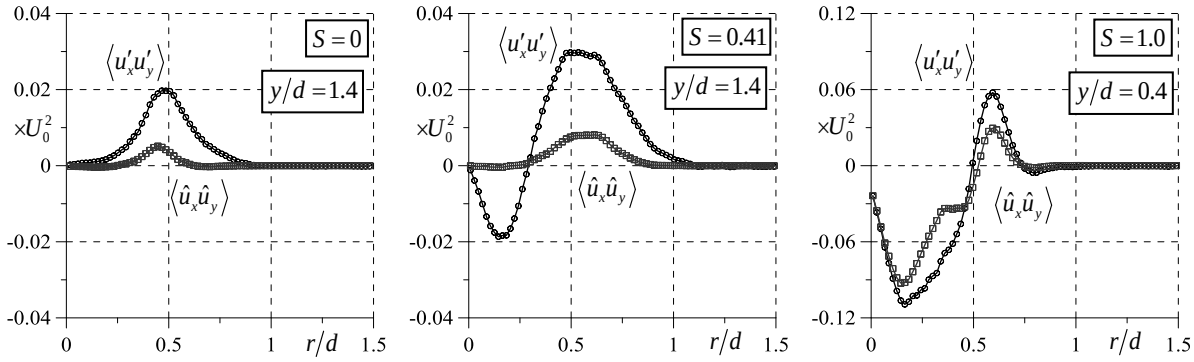

Figure 9. Profiles of the Reynolds stress for swirling jets and contribution of coherent velocity fluctuations

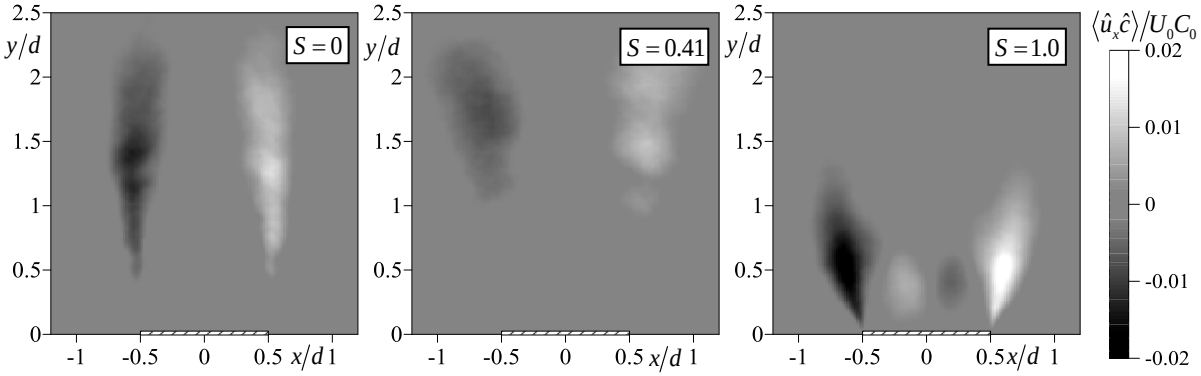

Figure 10. Contribution of coherent velocity and concentration fluctuations to the Reynolds flux for swirling jets

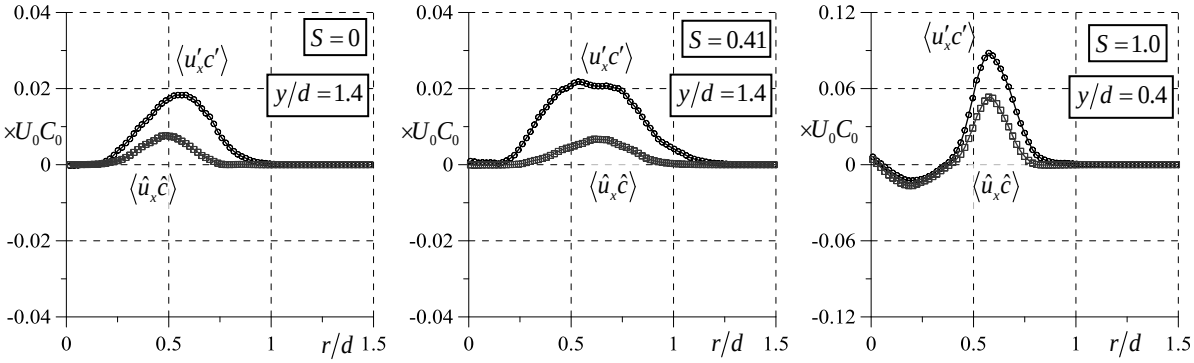

Figure 11. Profiles of the *x*-component of the Reynolds flux for swirling jets and contribution of coherent velocity and concentration fluctuations